RSC Advances

PAPER

View Article Online
View Journal | View Issue

Cite this: *RSC Adv.*, 2020, **10**, 9444

Eu^{3+}-based luminescence ratiometric thermometry

Leipeng Li,[a] Yuan Zhou,[a] Feng Qin,[b] Jipeng Miao,[a] Yangdong Zheng[a] and Zhiguo Zhang *[b]

Received 7th January 2020
Accepted 24th February 2020

DOI: 10.1039/d0ra00170h

rsc.li/rsc-advances

Recently, luminescence ratiometric thermometry has gained ever-increasing attention due to its merits of rapid response, non-invasiveness, high spatial resolution, and so forth. For research fields relying on temperature measurements, achieving a higher relative sensitivity of this measurement is still an important task. In this work, we developed a strategy for achieving a more sensitive temperature measurement, one merely depending on the photoluminescence of Eu^{3+}. We showed that using the $^5D_1$–$^7F_1$ transition and the hypersensitive $^5D_0$–$^7F_2$ transition of Eu^{3+} can boost the relative sensitivity compared with the method relying on the $^5D_1$–$^7F_1$ and $^5D_0$–$^7F_1$ transitions of Eu^{3+}. The difference between these two strategies was studied and was explained by the hypersensitive $^5D_0$–$^7F_2$ transition more steeply decreasing than the $^5D_0$–$^7F_1$ transition with a rise in temperature. Our work is expected to help researchers design sensitive optical thermometers *via* proper use of this hypersensitive transition.

1. Introduction

Temperature, one of the most significant physical and chemical parameters, plays a quite important role in several fields, spanning from biological medicine to industrial processes and other fields affecting our daily lives.[1] For instance, an increase of 3 °C in body temperature directly threatens human health. Therefore, developing novel and practical methods or devices for measuring temperature has become very important.[2–5] Although a traditional thermocouple and thermistor are widely used nowadays, they are not very good at measuring temperature precisely, quickly, and in particular, non-invasively. Optical thermometry can overcome these problems well as it features a short response time, non-contact work model, relatively high thermal and spatial resolutions, and so forth.[6–10]

So far, several approaches have been developed to realize optical thermometry. Of these, luminescence ratiometric thermometry has gained ever-increasing attention.[11] It depends on two emission lines and is thus strongly resistant to many influencing factors, such as the loss of optics transmission.[12] When first developed, luminescence ratiometric thermometry involved thermally coupled energy levels (TCELs) of rare earth and transition metal ions.[13–18] Sui *et al.* prepared a Tm^{3+}/Yb^{3+}-co-doped $LiYF_4$ single crystal and found that the intensity ratio between the $^3F_2/^3F_3$–$^3H_6$ and $^3H_4$–$^3H_6$ transitions of Tm^{3+} could be used for temperature determination.[19] Rakov *et al.* demonstrated that the $^2F_{5/2}$ Stark sublevels of Yb^{3+} and the $^4I_{13/2}$ Stark sublevels of Er^{3+} were both TCELs, based on which they successfully measured the temperature.[20,21] Marciniak *et al.* prepared $LiYbP_4O_{12}:Er^{3+}$ nanocrystals and showed that the intensity ratio between the $^2H_{11/2}$–$^4I_{15/2}$ and $^4S_{3/2}$–$^4I_{15/2}$ transitions of Er^{3+} followed the Boltzmann distribution, and could be used for measuring temperature.[22] Nikolić *et al.* demonstrated the potential application of Dy^{3+}-doped $GdVO_4$ as a thermographic phosphor, with this potential application based on the $^4I_{15/2}$ and $^4F_{9/2}$ states being TCELs.[23] Rai *et al.* observed the $^3P_1$–$^3H_5$ and $^3P_0$–$^3H_5$ transitions in Pr^{3+}-doped lithium tellurite glass and showed the luminescence intensity ratio (LIR) between them to be a promising temperature indicator.[24] Back *et al.* and Ueda *et al.* have shown the TCELs of Cr^{3+} also follow the Boltzmann distribution and thus can be used for ratiometric thermometry.[25–27] Recently, luminescence ratiometric thermometry was also realized using non-TCELs.[28–30] Cui *et al.* prepared the first ratiometric luminescent metal–organic framework thermometer on the basis of the green-light emission of Tb^{3+} and the red-light emission of Eu^{3+}.[31] Savchuk *et al.* proposed a new upconversion thermometry method based on emissions of light from Ho^{3+} and Tm^{3+}.[32] Cortelletti *et al.* showed that Nd^{3+}–Yb^{3+}-codoped SrF_2 nanoparticles with a multi-shell architecture, operating in the biological window, were qualified temperature indicators.[33] Nearly all of these reported investigations were committed to increasing the relative sensitivity of temperature measurements, which is one of the most important goals in the field of optical thermometry.

In this work, we developed a strategy for boosting the relative sensitivity of luminescence ratiometric thermometry. This strategy was based on the combination of a common transition and a hypersensitive transition of Eu^{3+}. We showed that the luminescence intensity ratio between the $^5D_1$–$^7F_1$ and $^5D_0$–$^7F_1$ transitions and the LIR between the $^5D_1$–$^7F_1$ and $^5D_0$–$^7F_2$

[a]School of Physics, Harbin Institute of Technology, Harbin, 150001, P.R. China
[b]School of Instrumentation Science and Engineering, Condensed Matter Science and Technology Institute, Harbin Institute of Technology, 92 West Dazhi Street, Nan Gang District, Harbin, Heilongjiang Province, 150001, P.R. China. E-mail: zhangzhiguo@hit.edu.cn; Fax: +86-451-86402639; Tel: +86-451-86402639

transitions of Eu^{3+} can be used for temperature measurements as both LIRs were found to increase gradually with increasing temperature. However, the latter LIR, compared with the former, showed a greater relative sensitivity. The discrepancy of sensitivity between these two temperature detection methods was especially obvious at relatively high temperatures. The mechanism for this phenomenon was studied in detail.

2. Materials and characterization

CaO, WO_3, and Eu_2O_3 (4N, Aladdin Co., Ltd) were used as raw materials. $CaWO_4 : X\%\ Eu^{3+}$ ($X = 1$, 10 and 20) phosphors were prepared by following a high-temperature solid state method. To synthesize the phosphors, first stoichiometric amounts of CaO, WO_3 and Eu_2O_3 raw materials were fully ground together in a 50 mL agate mortar, with the aim of forming uniform mixtures. These mixtures were then pressed into several disks for the subsequent optical tests, and the disks were sintered at 1473 K for 4 h to form the final products.

Powder X-ray diffraction (PXRD) patterns of the as-prepared samples were acquired (PANalytical X'Pert powder X-ray diffractometer) at room temperature. A continuous-wave 405 nm laser diode (ITC-510, Thorlabs) and 150 W xenon lamp (LHX-150, Zolix Instruments Co., Ltd) were used as excitation sources. A spectrometer (SBP-300, Zolix Instruments Co., Ltd) was used for wavelength discrimination. A photomultiplier (PMTH-S1-CR131, Zolix Instruments Co., Ltd) was used to collect excitation and emission spectra of the samples. The temperature of the samples was changed using a home-made heating chamber with an accuracy of ± 0.3 K over the experimental temperature range of 333 to 733 K.

3. Results and discussion

3.1 PXRD patterns and crystal structure

The expected structure of the as-prepared samples was confirmed using PXRD analysis (Fig. 1a). For comparison, the reference data set of JCPDS no. 41-1431 is also presented. The PXRD patterns acquired of the as-prepared samples were observed to be quite similar to the reference. Moreover, no redundant peaks were observed for the samples. These results revealed that the $CaWO_4 : X\%\ Eu^{3+}$ ($X = 1$, 10 and 20) phosphors were prepared successfully and each formed a pure tetragonal phase. The addition of Eu^{3+} did not affect the structure of $CaWO_4$. Eu^{3+} successfully occupied the Ca^{2+} site in the $CaWO_4$ host, apparently due to the similarity of the Eu^{3+} (0.095 nm) and Ca^{2+} (0.099 nm) radii. The crystal structure of the scheelite-type $CaWO_4$ is also given (Fig. 1b). The Eu^{3+}/Ca^{2+} ions embedded in the phosphors were each octahedrally coordinated by eight O^{2-} oxygens (Fig. 1c). Moreover, the W^{6+} ions in the samples were each surrounded by four O^{2-} oxygens (Fig. 1d), forming a tetrahedron.

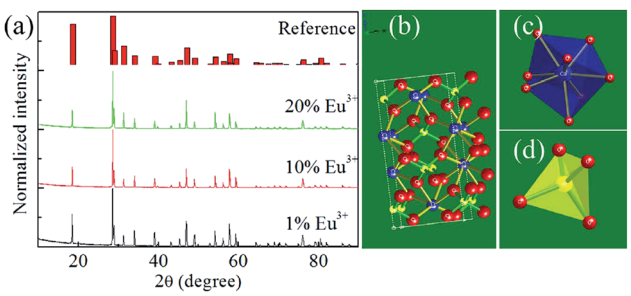

Fig. 1 (a) PXRD patterns of the as-prepared samples. (b) Crystal structure, (c) [CaO_8] cluster and (d) [WO_4] cluster of the Scheelite-type $CaWO_4$.

3.2 Basic spectroscopic properties

A room-temperature photoluminescence (PL) spectrum of the $CaWO_4$:10%Eu^{3+} phosphors excited with 405 nm-wavelength light was acquired (Fig. 2a). Between wavelengths of 500 and 750 nm, six PL bands with peaks at wavelengths of 535, 580, 593, 615, 650 and 700 nm, respectively, were observed. The 535 nm PL band arose from the $^5D_1$–$^7F_1$ transition of Eu^{3+}, and the 580, 593, 615, 650 and 700 nm PL bands were attributed, respectively, to the $^5D_0$–^7F_J ($J = 0$, 1, 2, 3 and 4) transitions of Eu^{3+}.[34–39] The 615 nm PL band originating from the hypersensitive transition was the most intense band, a result similar to that reported previously.[34–39] By monitoring this PL band, the excitation spectrum was collected (Fig. 2a). All of these excitation bands were sharp. The attributions of these bands have been described previously.[34–39] According to a proposed model, upon excitation at 405 nm, the Eu^{3+} ions at the ground state absorbed these photons and adopted each a high-energy excited state (Fig. 2b). This process was then followed by non-radiative relaxation to the lower-energy $^5D_1$ and $^5D_0$ emitting states. Finally, radiative transitions from these two excited states to the different ground states occurred.

A series of $CaWO_4 : X\%\ Eu^{3+}$($X = 1$, 10, 20) phosphors were prepared. For all of the samples, the characteristic PL bands of Eu^{3+} were observed. The profile and position of these PL bands remained unchanged as the concentration of Eu^{3+} was changed (Fig. 3a). However, as the Eu^{3+} concentration was increased, the PL band intensity of Eu^{3+} increased sharply, due to more Eu^{3+} ions acting as luminescence centres. However, when the Eu^{3+} concentration was increased tenfold, the enhancement of the

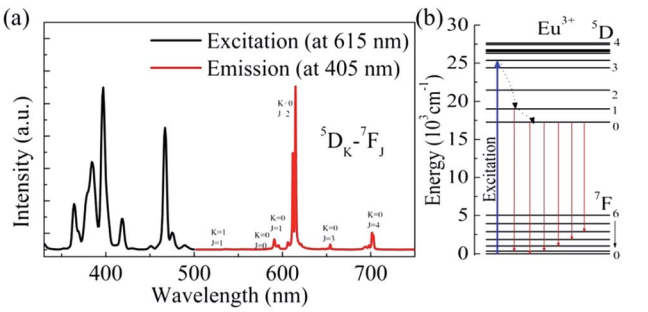

Fig. 2 (a) Room-temperature excitation spectrum (monitored at 615 nm) and PL spectrum (excitation at 405 nm) of the $CaWO_4$:10%Eu^{3+} phosphors. (b) Energy level diagram of Eu^{3+} and possible excitation–emission processes.

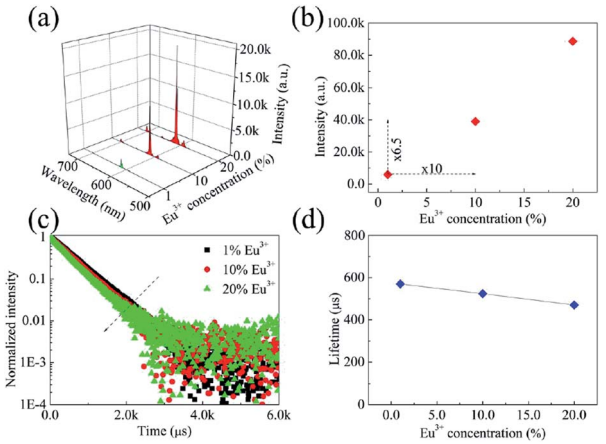

Fig. 3 (a) Room-temperature PL spectra, (b) integrated emission intensities, (c) room-temperature decay curves, and (d) lifetimes of the 615 nm PL band of the phosphors.

total emission intensity of the phosphors did not keep pace (Fig. 3b). The concentration quenching effect was expected to play a significant role.

Room-temperature decay curves of the 615 nm PL band of the prepared phosphors were collected (Fig. 3c). All of the decay curves were modelled effectively using the single exponential function

$$I(t) = I(0)\exp\left(-\frac{t}{t_0}\right), \quad (1)$$

where I is the intensity of the PL decay curve, t is time and t_0 is the lifetime. By using this equation, the lifetimes of the 615 nm PL band were calculated for the prepared phosphors at room temperature (Fig. 3d). As the Eu^{3+} concentration was increased from 1 to 20%, the lifetime of the 615 nm PL band decreased gradually from 569 to 470 μs, indicating the presence of a concentration quenching effect shortening the lifetimes of the emitting states.

Room-temperature PL spectra of the as-prepared phosphors excited with light of a wavelength of 405 nm were acquired (Fig. 4a). Note that they were normalized to the PL intensity at 615 nm. The LIR between the 615 and 593 nm PL bands was obtained (inset in Fig. 4a). As has been described previously, the 615 nm PL band arose from the $^5D_0$–$^7F_2$ transition, which has been confirmed to be a hypersensitive transition. Due to this unique characteristic, the 615 nm PL band was sensitive to the symmetry property of the Eu^{3+} site in the $CaWO_4$ host. Therefore, the LIR between the 615 and 593 nm PL bands reflected the distortion of the crystal field environment around Eu^{3+}.[35] There was a slight fluctuation of the LIR between the 615 and 593 nm PL bands, demonstrating a lack of any effect of Eu^{3+} concentration on the symmetry properties of the Eu^{3+} site in the $CaWO_4$ host. The CIE chromaticity coordinates of the prepared phosphors were also calculated based on their emission spectra (Fig. 4b). The emissions of all of these phosphors were located in the red region, as the 615 nm PL band in each case was the predominant band in the emission spectrum. Moreover, as the Eu^{3+} concentration was increased, the CIE chromaticity coordinates gradually became located closer to the deep-red region. This result may be explained as follows: as the Eu^{3+} concentration was increased, the population of the $^5D_0$ state increased, at the expense of a depopulation of the upper $^5D_1$ state, due to the concentration quenching effect; and therefore, the red transition accounted for an increasing proportion of the total emission from the phosphors with increasing Eu^{3+} concentration.

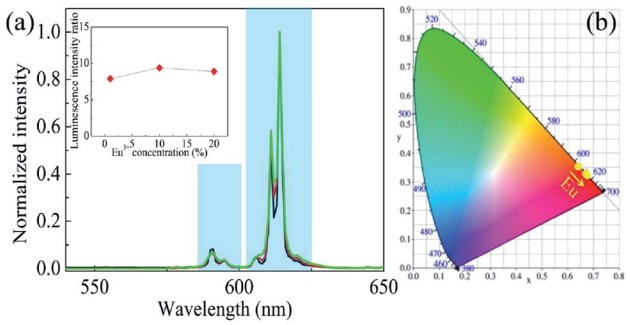

Fig. 4 (a) Normalized room-temperature PL spectra of the prepared $CaWO_4$: X% Eu^{3+}(X = 1, 10, 20) phosphors, and the LIR between the 615 and 593 nm PL bands as a function of Eu^{3+} concentration (inset). (b) CIE chromaticity coordinates of the prepared phosphors.

3.3 Temperature sensing properties

PL spectra were acquired of the as-prepared phosphors excited at 397 nm at various temperatures between 333 and 733 K (Fig. 5a and b). The integrated emission intensities of the 535, 593 and 615 nm PL bands were also calculated (Fig. 5c, d and e). The 535 nm PL band intensity was observed to increase as the temperature was increased from 333 to 453 K, and then decrease continuously with further increasing temperature. In contrast, the 593 and 615 nm PL band intensities each decreased markedly and continuously as the temperature was increased over the whole temperature range. This set of results can be understood by considering that the 535 nm PL band arose from the $^5D_1$ state while the other two PL bands were from the $^5D_0$ state: as there was a thermal equilibrium between the $^5D_1$ and $^5D_0$ states, the upper $^5D_1$ state became populated gradually at the expense of the lower $^5D_0$ state. Note that the decreased 535 nm PL band intensity at relatively high temperatures was likely due to an effect of thermal quenching.

The CIE chromaticity coordinates of the as-prepared phosphors were also calculated as a function of temperature from 333 to 733 K (Fig. 5e). At 333 K, the CIE chromaticity coordinates were determined to be located in the red region. As the temperature was increased, the 615 nm PL band became weaker. In contrast, the 535 nm PL band accounted for an increasing proportion of the total emission for the phosphors. Therefore, the CIE chromaticity coordinates gradually moved to the red region.

The LIR between the 535 and 593 nm PL bands (LIR-12) and that between the 535 and 615 nm PL bands (LIR-13) were obtained as a function of temperature from 333 to 733 K (Fig. 6a). Both LIRs were observed to increase monotonically with increasing temperature, with this result due to the thermal coupling between the $^5D_1$ and $^5D_0$ states. That is, both LIRs can

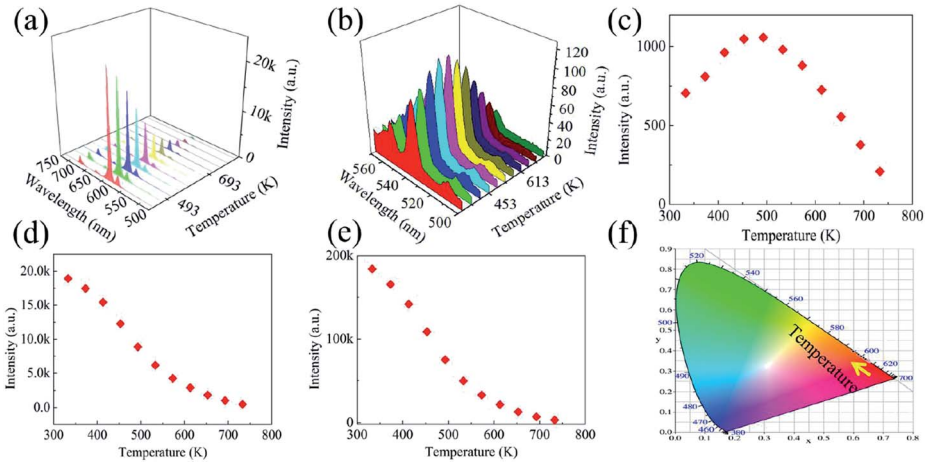

Fig. 5 (a and b) PL spectra, (c–e) integrated intensities of the (c) 535 nm, (d) 593 nm, and (e) 615 nm PL bands, and (f) CIE diagram of the as-prepared phosphors excited with light of a wavelength of 397 nm, each as a function of temperature from 333 to 733 K.

be used for indicating temperature. According to the Boltzmann distribution, the LIR between TCELs is expressed as[12]

$$\mathrm{LIR} = A\exp\left(-\frac{\Delta E}{kT}\right) + B, \tag{2}$$

where A is a constant, ΔE is the energy gap between TCELs, k is the Boltzmann constant, T is the absolute temperature and B is the fitting offset. Both LIR-12 and LIR-13 were fitted well by using eqn (2) (Fig. 6a). For LIR-12, the parameters A, ΔE and B were found to be 8.4, 1538 cm^{-1} and 0.024, respectively. The fitted energy gap was slightly smaller than the experimentally determined value. This discrepancy has been reported many times, and an explanation for it is still being pursued. For LIR-13, the fitted parameters A, ΔE and B were 1.9, 1762 cm^{-1} and 0.027, respectively. Obviously, the 593 and 615 nm PL bands showed different responses to temperature, and the intensity of the latter decreased more sharply with increasing temperature than that of the former.

To confirm the discrepancy between these two PL bands, the LIR between the 615 and 593 nm PL bands (LIR-32) was also calculated as a function of temperature from 333 to 733 K (Fig. 6b). LIR-32 was observed to drop sharply as the temperature was increased. At 733 K, LIR-32 was only ~70 percent of that at 333 K. This result revealed again a steeper response of the 615 nm PL band than of the 593 nm PL band to temperature. As mentioned above, LIR-32 can reflect the crystal field environment around Eu^{3+}. Therefore, the LIR-32 results, shown in Fig. 6b, suggested an increase in the symmetry of the Eu^{3+} site in the $CaWO_4$ host with increasing temperature.

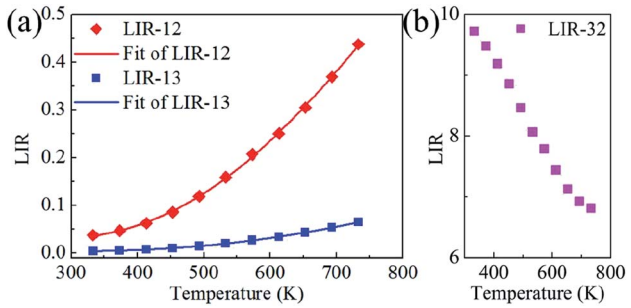

Fig. 6 (a) LIR-12, LIR-13 and (b) LIR-32 as a function of temperature from 333 to 733 K.

In order to obtain the relative sensitivity S_r, the absolute sensitivity S_a was calculated first according to the equation $S_r = S_a/\mathrm{LIR}$, with the absolute sensitivity S_a defined using the equation[40]

$$S_a = \frac{d\mathrm{LIR}}{dT}. \tag{3}$$

By using this equation, the absolute sensitivity S_a was calculated for LIR-12 and LIR-13 as a function of temperature from 333 to 733 K (Fig. 7a). LIR-12 showed an obviously larger S_a than did LIR-13. Based on the expression $S_r = S_a/\mathrm{LIR}$, the relative sensitivity S_r was also computed for LIR-12 and LIR-13 (Fig. 7b). The S_r for LIR-13 was calculated for each temperature value tested to be larger than that for LIR-12. This result may have been due to the 615 nm PL band originating from the hypersensitive transition and thus being more sensitive to the surroundings. With an increase in temperature, the symmetry of the Eu^{3+} site also increased, which resulted in a more serious decrease in the intensity of the 615 nm PL band than of the intensity of the 593 nm PL band.

The temperature resolution ΔT, in addition to the relative sensitivity S_r, is also very important in practice. It is defined as

$$\Delta T = \frac{\Delta\mathrm{LIR}/\mathrm{LIR}}{S_r}. \tag{4}$$

where ΔLIR/LIR is the relative uncertainty of the LIR that is used for indicating temperature. The terms ΔLIR-12/LIR-12 and ΔLIR-13/LIR-13 can be expressed as

$$\Delta\mathrm{LIR\text{-}12}/\mathrm{LIR\text{-}12} = \sqrt{\left(\frac{\Delta I_1}{I_1}\right)^2 + \left(\frac{\Delta I_2}{I_2}\right)^2}. \tag{5}$$

and

$$\Delta\mathrm{LIR\text{-}13}/\mathrm{LIR\text{-}13} = \sqrt{\left(\frac{\Delta I_1}{I_1}\right)^2 + \left(\frac{\Delta I_3}{I_3}\right)^2}, \tag{6}$$

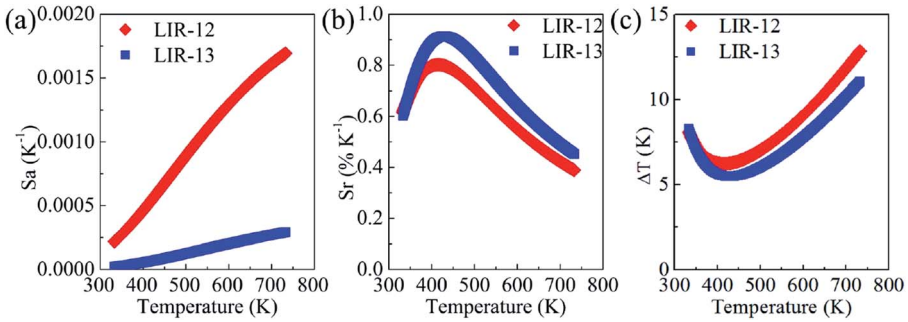

Fig. 7 (a) Absolute sensitivities, (b) relative sensitivities and (c) temperature resolutions for LIR-12 and LIR-13 as a function of temperature from 333 to 733 K.

where in the current work I_1, I_2 and I_3 were used to denote the intensities of the 535, 593 and 615 nm PL bands, respectively. Under the same experimental setup, $\Delta I_3/I_3$ was always lower in value than was $\Delta I_2/I_2$, due to the higher intensity of the 615 nm PL band. Inspection of the emission spectra of the samples clearly showed a much larger value for $\Delta I_1/I_1$ than for $\Delta I_2/I_2$ and $\Delta I_3/I_3$. Therefore, the value of ΔLIR-13/LIR-13 was just slightly lower than that of ΔLIR-12/LIR-12. The S_r for LIR-13 was shown above to be greater than that for LIR-12. So, the strategy of using 535 and 615 nm PL bands yielded a better temperature resolution than did the strategy depending on the 535 and 593 nm PL bands (Fig. 7c). Therefore, using the 535 and 615 nm PL bands was shown to achieve not only a higher relative sensitivity but also a better temperature resolution than that achieved using the 535 and 593 nm PL bands.

4. Conclusion

In summary, Eu^{3+}-embedded scheelite-type phosphors were prepared. Upon excitation at 405 nm, the characteristic $^5D_1$–$^7F_1$, $^5D_0$–$^7F_1$ and $^5D_0$–$^7F_2$ transitions of Eu^{3+} were observed for the as-prepared samples. It was shown that both LIR-12 and LIR-13 can be used for indicating temperature. Moreover, LIR-13 showed a larger relative sensitivity than LIR-12. The discrepancy between these two temperature detection methods was disclosed, and was ascribed to a faster decay of the $^5D_0$–$^7F_2$ transition than of the $^5D_0$–$^7F_1$ transition with increasing temperature, further demonstrating a gradually increasing symmetry around Eu^{3+} in the $CaWO_4$ host with increasing temperature. Our work, by revealing the proper use the hypersensitive transition, is expected to help researchers design sensitive optical thermometry.

Conflicts of interest

The authors declare no competing financial interests.

Acknowledgements

This work was supported by the National Natural Science Foundation of China (NSFC) (Grant No. 81571720 & 61505045).

References

1 P. R. N. Childs, J. R. Greenwood and C. A. Long, *Rev. Sci. Instrum.*, 2000, **71**, 2959–2978.
2 M. Quintanilla and L. M. Liz-Marzán, *Nano Today*, 2018, **19**, 126–145.
3 D. Jaque and F. Vetrone, *Nanoscale*, 2012, **4**, 4301–4326.
4 J. Rocha, C. D. S. Brites and L. D. Carlos, *Chem.–Eur. J.*, 2016, **22**, 1–15.
5 X. Wang, O. S. Wolfbeis and R. J. Meier, *Chem. Soc. Rev.*, 2013, **42**, 7834–7869.
6 F. Vetrone, R. Naccache, A. Zamarrón, A. J. de la Fuente, F. Sanz-Rodríguez, L. M. Maestro, E. M. Rodriguez, D. Jaque, J. G. Solé and J. A. Capobianco, *ACS Nano*, 2010, **4**, 3254–3258.
7 L. Marciniak, K. Prorok and A. Bednarkiewicz, *J. Mater. Chem. C*, 2017, **5**, 7890–7897.
8 R. Lei, D. Deng, X. Liu, F. Huang, H. Wang, S. Zhao and S. Xu, *Opt. Mater. Express*, 2018, **8**, 3023–3035.
9 S. Zhou, C. Duan, M. Yin, X. Liu, S. Han, S. Zhang and X. Li, *Opt. Express*, 2018, **26**, 27339–27345.
10 B. Dong, D. P. Liu, X. J. Wang, T. Yang, S. M. Miao and C. R. Li, *Appl. Phys. Lett.*, 2007, **90**, 181117.
11 S. Balabhadra, M. L. Debasu, C. D. S. Brites, L. A. O. Nunes, O. L. Malta, J. Rocha, M. Bettinellie and L. D. Carlos, *Nanoscale*, 2015, **7**, 17261–17267.
12 S. A. Wade, S. F. Collins and G. W. Baxter, *J. Appl. Phys.*, 2003, **94**, 4743–4756.
13 M. D. Dramićanin, *Methods Appl. Fluoresc.*, 2016, **4**, 042001.
14 M. Back, J. Ueda, J. Xu, D. Murata, M. G. Brik and S. Tanabe, *ACS Appl. Mater. Interfaces*, 2019, **11**, 38937–38945.
15 S. Liu, H. Ming, J. Cui, S. Liu, W. You, X. Ye, Y. Yang, H. Nie and R. Wang, *J. Phys. Chem. C*, 2018, **122**, 16289–16303.
16 H. Suo, C. Guo, J. Zheng, B. Zhou, C. Ma, X. Zhao, T. Li, P. Guo and E. M. Goldys, *ACS Appl. Mater. Interfaces*, 2016, **8**, 30312–30319.
17 B. Dong, R. N. Hua, B. S. Cao, Z. P. Li, Y. Y. He, Z. Y. Zhang and O. S. Wolfbeis, *Phys. Chem. Chem. Phys.*, 2014, **16**, 20009–20012.
18 L. Tong, X. Li, J. Zhang, S. Xu, J. Sun, H. Zheng, Y. Zhang, X. Zhang, R. Hua, H. Xia and B. Chen, *Opt. Express*, 2017, **25**, 16047–16058.

19 G. Sui, B. Chen, J. Zhang, X. Li, S. Xu, J. Sun, Y. Zhang, L. Tong, X. Luo and H. Xia, *J. Lumin.*, 2018, **198**, 77–83.
20 N. Rakov and G. S. Maciel, *Opt. Lett.*, 2014, **39**, 3767–3769.
21 N. Rakov and G. S. Maciel, *J. Lumin.*, 2018, **199**, 293–297.
22 L. Marciniak, K. Waszniewska, A. Bednarkiewicz, D. Hreniak and W. Strek, *J. Phys. Chem. C*, 2016, **120**, 8877–8882.
23 M. G. Nikolić, D. J. Jovanović and M. D. Dramićanin, *Appl. Opt.*, 2013, **52**, 1716–1724.
24 V. K. Rai, D. K. Rai and S. B. Rai, *Sens. Actuators, A*, 2006, **128**, 14–17.
25 M. Back, E. Trave, J. Ueda and S. Tanabe, *Chem. Mater.*, 2016, **28**, 8347–8356.
26 M. Back, J. Ueda, M. G. Brik, T. Lesniewski, M. Grinberg and S. Tanabe, *ACS Appl. Mater. Interfaces*, 2018, **10**, 41512–41524.
27 J. Ueda, M. Back, M. G. Brik, Y. Zhuang, M. Grinberg and S. Tanabe, *Opt. Mater.*, 2018, **85**, 510–516.
28 D. Chen, W. Xu, S. Yuan, X. Li and J. Zhong, *J. Mater. Chem. C*, 2017, **5**, 9619–9628.
29 L. Marciniak, A. Bednarkiewicz, J. Drabik, K. Trejgis and W. Strek, *Phys. Chem. Chem. Phys.*, 2017, **19**, 7343–7351.
30 K. Trejgis and L. Marciniak, *Phys. Chem. Chem. Phys.*, 2018, **20**, 9574–9581.
31 Y. Cui, H. Xu, Y. Yue, Z. Guo, J. Yu, Z. Chen, J. Gao, Y. Yang, G. Qian and B. Chen, *J. Am. Chem. Soc.*, 2012, **134**, 3979–3982.
32 O. A. Savchuk, J. J. Carvajal, C. D. S. Brites, L. D. Carlos, M. Aguilo and F. Diaz, *Nanoscale*, 2018, **10**, 6602–6610.
33 P. Cortelletti, A. Skripka, C. Facciotti, M. Pedroni, G. Caputo, N. Pinna, M. Quintanilla, A. Benayas, F. Vetrone and A. Speghini, *Nanoscale*, 2018, **10**, 2568–2576.
34 D. Tu, W. Zheng, P. Huang and X. Chen, *Coord. Chem. Rev.*, 2019, **378**, 104–120.
35 Y. Su, L. Li and G. Li, *Chem. Mater.*, 2008, **20**, 6060–6067.
36 Y. Chen, S. W. Park, B. K. Moon, B. C. Choi, J. H. Jeong and C. Guo, *CrystEngComm*, 2013, **15**, 8255–8261.
37 X.-J. Zhang, *J. Mater. Sci.: Mater. Electron.*, 2014, **25**, 5496–5500.
38 J. Han, C. McBean, L. Wang, C. Jaye, H. Liu, D. A. Fischer and S. S. Wong, *J. Phys. Chem. C*, 2015, **119**, 3826–3842.
39 S. P. Culver and R. L. Brutchey, *Dalton Trans.*, 2016, **45**, 18069–18073.
40 R. Lei, D. Deng, X. Liu, F. Huang, H. Wang, S. Zhao and S. Xu, *Opt. Mater. Express*, 2018, **8**, 3023–3035.